Electronic Supplementary Material (ESI) for Inorganic Chemistry Frontiers.

Supporting Information for **"Exfoliated Clay Nanosheet as an Efficient Additive for Improving the Electrode Functionality of Graphene-based Nanocomposite**"

*Kanyaporn Adpakpang, Seung Mi Oh, Boyeon Park, and Seong-Ju Hwang**

Fig. S1. (Left) Zeta potential curves and (right) photoimages of the colloidal suspensions of (a) graphene oxide (G-O), (b) exfoliated laponite clay nanosheet, (c, d, e) the mixtures of G-O with exfoliated laponite clay nanosheets (1, 2.5, and 5wt%), respectively.

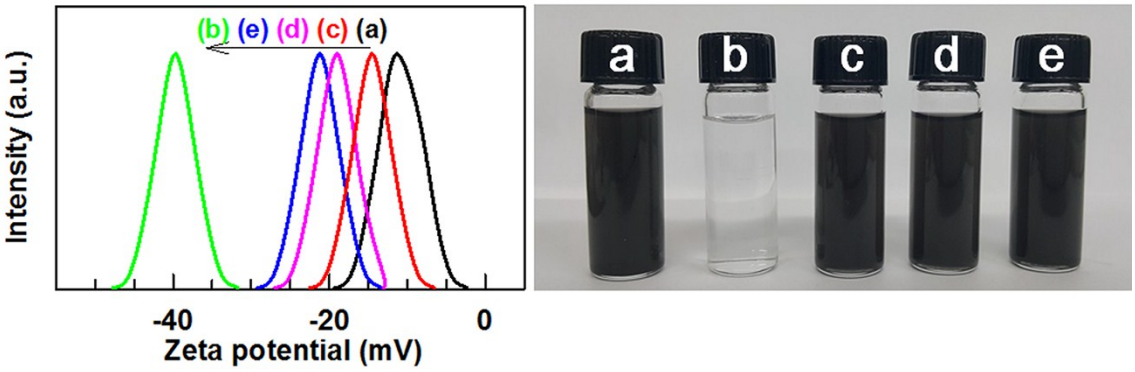

: As presented in the left panel of **Fig. S1**, both the G-O and exfoliated laponite clay nanosheets possess negative surface charge. The mixing of both the nanosheets leads to the formation of stable colloidal mixtures with similar negative surface charges. The marked colloidal stabilities of the obtained mixed suspensions are confirmed by the photoimages in the right panel of **Fig. S1**. The resulting colloidal mixtures of both the nanosheets can be used as efficient precursors for the immobilization of Mn_3O_4 nanoparticles.

Fig. S2. Photoimage for the product after hydrothermal treatment at 150 °C for 3 h.

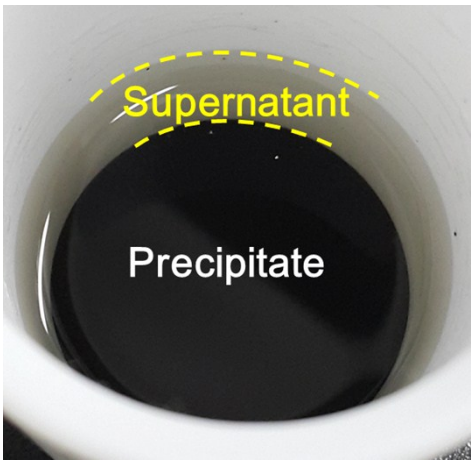

: As shown in **Fig. S2**, the transparent supernatant solution is obtained with dark-colored precipitate after the hydrothermal reaction. This observation clearly demonstrates the complete incorporation of both clay and reduced graphene oxide (rG-O) nanosheets into the precipitated nanocomposite.

Fig. S3. Field emission-scanning electron microscopy (FE-SEM) image of the Mn_3O_4–clay nanocomposite.

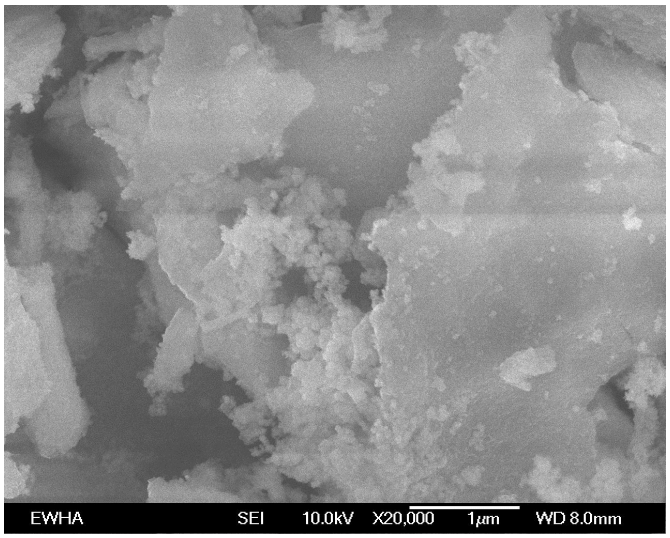

: As depicted in **Fig. S3**, the graphene-free Mn_3O_4–clay nanocomposite was also synthesized by the same procedure as that for the synthesis of Mn_3O_4–N-doped rG-O–clay (**MGC)** nanocomposites except for the absence of graphene. The obtained material shows the porous stacking structure of nanosheets with the deposition of Mn_3O_4 nanocrystals on the nanosheet surface. This result clearly demonstrates that the Mn_3O_4 nanocrystals can be effectively immobilized on the surface of exfoliated clay nanosheet, highlighting an efficient role of exfoliated clay nanosheet as a substrate for the growth of Mn_3O_4 nanoparticles.

Fig. S4. (Top) FE-SEM images and (bottom) N_2 adsorption–desorption isotherms of N-doped rG-O–clay nanocomposites with the clay contents of (a) 0, (b) 1, (c) 2.5, and (d) 5wt%.

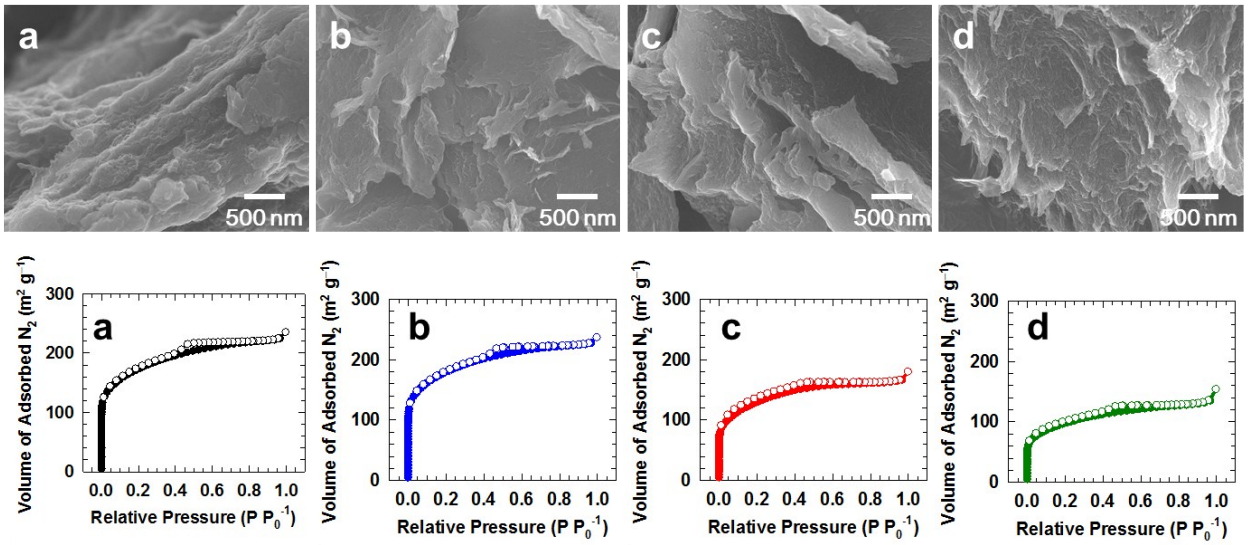

: As can be seen clearly from the FE-SEM images in the top panel of **Fig. S4**, the N-doped graphene–clay nanocomposites with variable clay contents exhibit highly porous stacking morphologies, which is attributable to the absence of pore-blocking Mn_3O_4 nanoparticles. As shown in the bottom panel of **Fig. S4**, all the N_2 adsorption–desorption isotherms of the present nanocomposites commonly display a combined type I/IV hysteresis, indicating the formation of both micropores and mesopores. The BET surface areas of the present materials are determined to be 570, 586, 435, and 327 $m^2\ g^{-1}$ for the materials with the clay contents of 0, 1, 2.5, and 5wt%, respectively, which are much greater than those of **MGC** nanocomposites. This result strongly suggests that the pore blocking by the immobilized Mn_3O_4 nanoparticles is mainly responsible for the relatively small surface areas of **MGC** nanocomposites. The BET surface area of the restacked N-doped rG-O nanosheets becomes greater upon the incorporation of clay nanosheet at 1wt%. However, a further increase of clay content leads to the depression of

surface area, which is attributable to the intrinsically smaller surface area of clay nanosheet than rG-O. The effect of clay addition on the pore structure of nanocomposite can be further studied by the evolution of pore structure. The addition of clay nanosheet results in the depression of the micropore of Mn_3O_4–rG-O nanocomposite. Since micropores of the present nanocomposites mainly originate from the defects in N-doped rG-O domains and the stacking structure of graphene sheet, the decrease of micropore with increasing the clay content is indicative of the defect-curing of N-doped rG-O and the prevention of the regular stacking structure of graphene upon the intervention of clay nanosheet in-between graphene nanosheets.

Fig. S5. TEM images of (a–c) exfoliated clay nanosheet and (d) exfoliated G-O nanosheet.

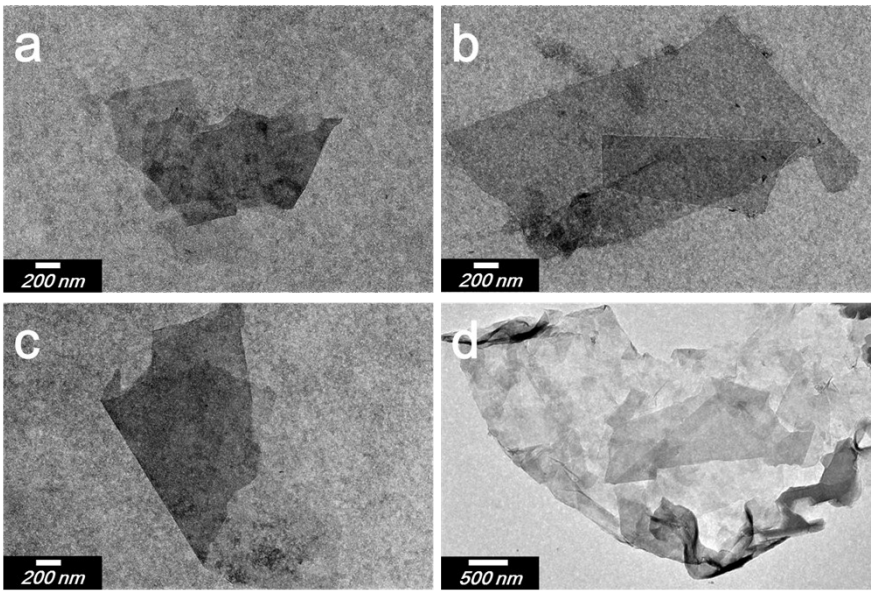

: The lateral dimensions of clay and G-O nanosheets are determined with the TEM analysis. As shown in **Fig. S5**, the exfoliated clay nanosheet possesses the lateral dimension of hundred nanometers to micrometers, which is similar to that of G-O nanosheet. The similar lateral dimensions of clay and G-O nanosheets are effective in achieving the significant variation of the pore structure of nanocomposite upon the addition of clay nanosheet.

Fig. S6. (Left) C 1s and (right) N 1s X-ray photoelectron spectra (XPS) of (a) G-O, (b) **MGC0**, (c) **MGC1**, (d) **MGC2.5**, and (e) **MGC5**.

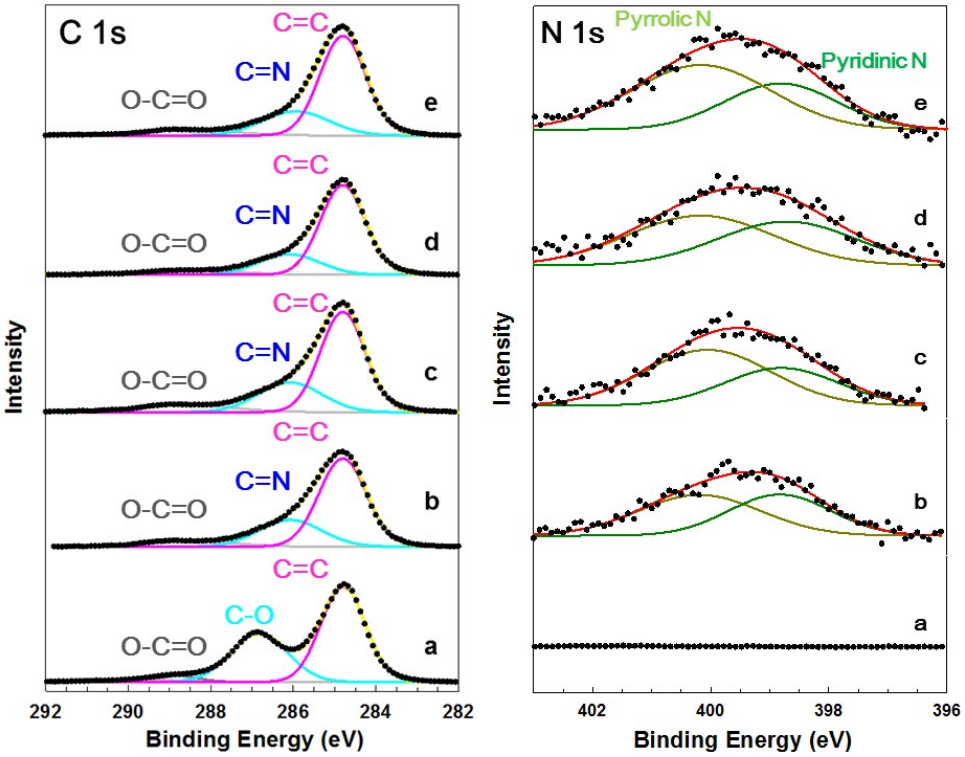

: As shown in the left panel of **Fig. S6**, the C 1s XPS data of all the **MGC** nanocomposites exhibit the reduction of the peaks related to the oxygen functional group at high binding energies with the advent of new peak corresponding to (C–N) bond, confirming the reduction of graphene oxide (G-O) to form rG-O and the incorporation of N atom into the rG-O structure. The presence of the pyrrolic and pyridinic N species in the present nanocomposites is confirmed by N 1s XPS spectra presented in the right panel of **Fig. S6**.

Fig. S7. Charge–discharge capacity plot of exfoliated clay nanosheet as anode materials for LIBs at the current density of 200 mA g^{-1}.

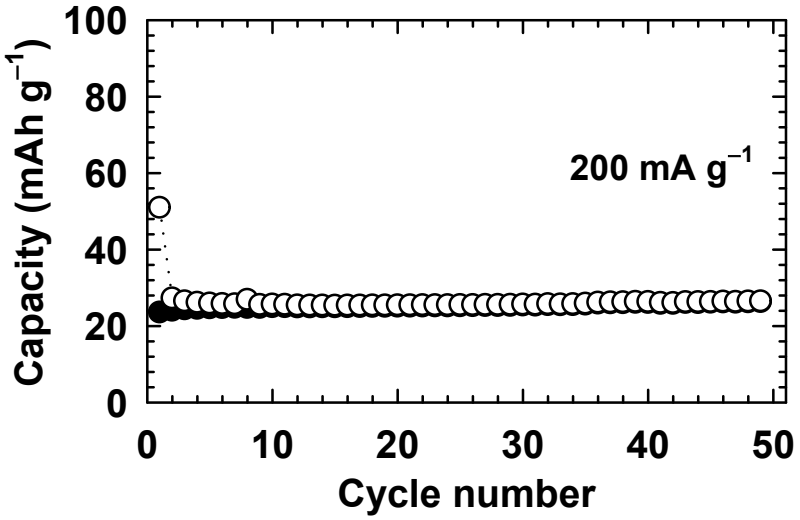

: As shown in **Fig. S7**, the exfoliated clay nanosheet exhibits a reversible charge–discharge capacity of ~26 mAh g^{-1} at the current density of 200 mA g^{-1}, which is much smaller than those of the present **MGC** nanocomposites. Based on this result, the remarkable increase of the electrode activity of Mn_3O_4–graphene nanocomposite upon the addition of clay nanosheet is attributable to the synergistic effect of hybridization between clay and graphene on composite structure and charge transport kinetics not to the simple addition of the charge capacity of incorporated clay nanosheet.

Fig. S8. Coulombic efficiency (CE) plots of (a) **MGC0**, (b) **MGC1**, (c) **MGC2.5**, and (d) **MGC5**.

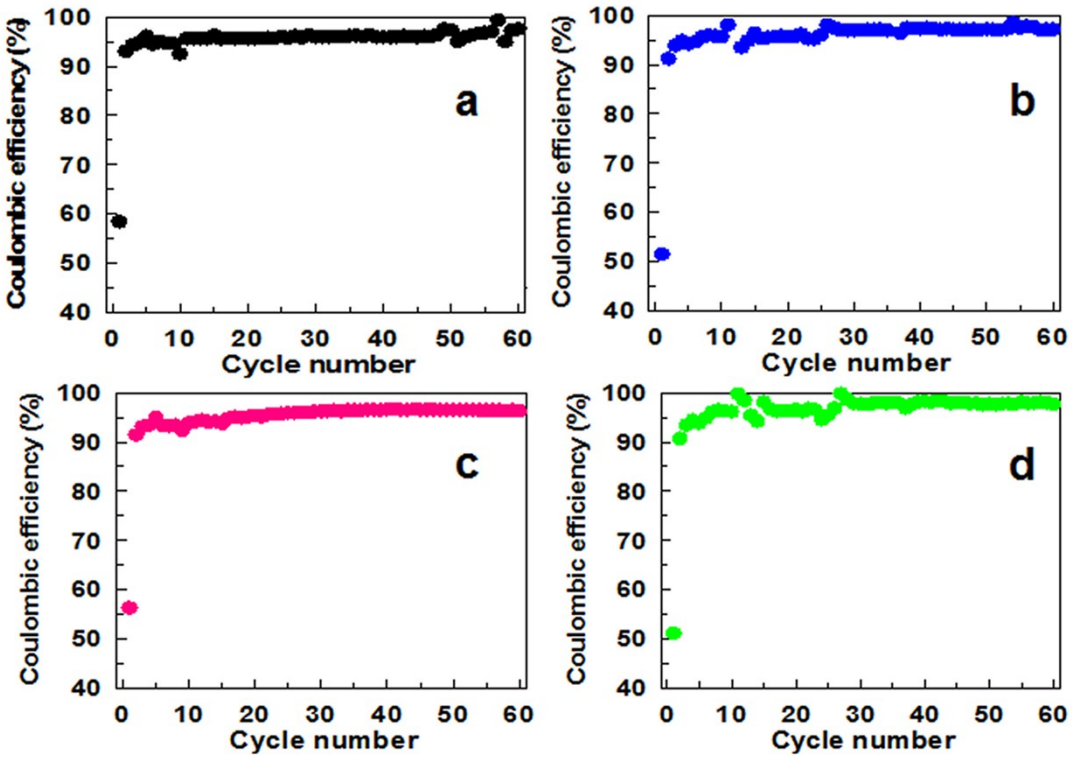

: As shown in **Fig. S8**, all the **MGC** nanocomposites commonly exhibit relatively low CE of ~50–66% at the first cycle. After a few initial cycles, the CE gradually increases to above 95% and then becomes stable for the following cycles. The initial capacity loss can be ascribed to the formation of irreversible solid-electrolyte-interface (SEI) layer and the following stabilization of CE reflects the formation of tolerable pore structure for repeated lithiation–delithiation processes.

Fig. S9. Differential capacity curves of (a) **MGC0**, (b) **MGC1**, (c) **MGC2.5**, and (d) **MGC5** nanocomposites for the 1st (black), 2nd (blue), 10th (red), and 60th (green) cycles.

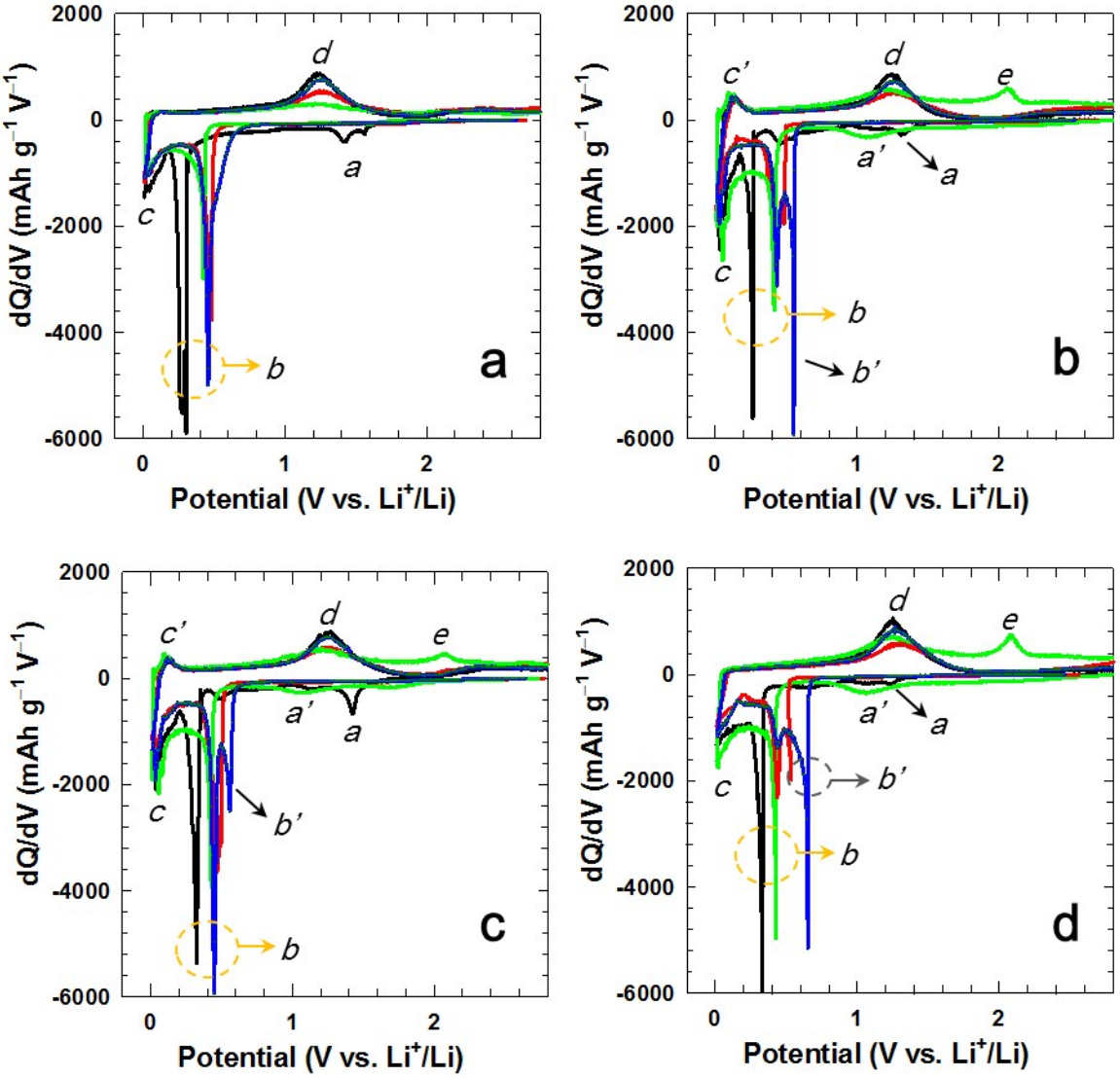

: To insightfully investigate the effect of the incorporation of clay nanosheet on the electrode activity of the **MGC** electrodes, differential capacity curves are plotted in **Fig. S9**. Like the charge–discharge profiles, all the **MGC** electrodes show the peaks at ~1.4 and ~0.3 V for the first discharging and the peak at 1.25 V for the first charging cycle. Additionally, all the **MGC**

electrodes exhibit the discharging peak at ~0.01 V, which is related to the insertion of lithium ions into graphene sheets and also the interfacial storage of lithium ions at the polymeric gel film on the surface of Mn(0) nanoparticles. Only the **MGC1** and **MGC2.5** electrodes show the charging peak at 0.13 V corresponding to the deinsertion of lithium ions from the graphene sheet, suggesting the reversible reaction of lithium ions with graphene for these materials. At the 2^{nd} discharging cycle, the potential of the reduction peak of MnO to Mn becomes elevated from 0.3 to 0.45 V. The peak intensities of **MGC0** and **MGC2.5** are greater than those of **MGC1** and **MGC5**. Additionally, the peak at 0.55 V (0.65 V for **MGC5**) is discernible for all the clay-incorporated electrodes. This peak is related to the irreversible reaction of lithium ions and SiO_2 forming Si nano-domains in the Li_4SiO_4/Li_2O matrix. This peak is more intense for the **MGC1** and **MGC5** than for the **MGC2.5**. This finding highlights that the optimization of electrode structure and interfacial composition via the incorporation of clay nanosheet plays an important role in improving the electrode activity of the clay-incorporated electrodes. As the cycling extends to the 60^{th} cycle, the reduction peak at ~0.55 V related to the redox process of SiO_2 disappears, reflecting the irreversible contribution of silica component. Conversely, the discharging peak at 1 V and charging peak at 2.1 V are still observable, which are related to the formation and reversible redox process of the high-valent manganese ions (Mn^{3+}/Mn^{4+}). These features are more distinct for the **MGC1** and **MGC5** electrodes than for the other homologues. The present findings strongly suggest that the initial capacity fading of clay-incorporated nanocomposites is mainly attributed to the irreversible contribution of SiO_2 component. Also, a gradual increase of the capacity with extending the cycles is ascribed to the reversible formation of higher valent Mn ions as well as the gradual improvement of the diffusion paths of Li ions.

Fig. S10. (Top) FE-SEM images and (bottom) powder X-ray diffraction (XRD) patterns for the electrochemically-cycled derivatives of (a) **MGC0**, (b) **MGC1**, (c) **MGC2.5**, and (d) **MGC5**.

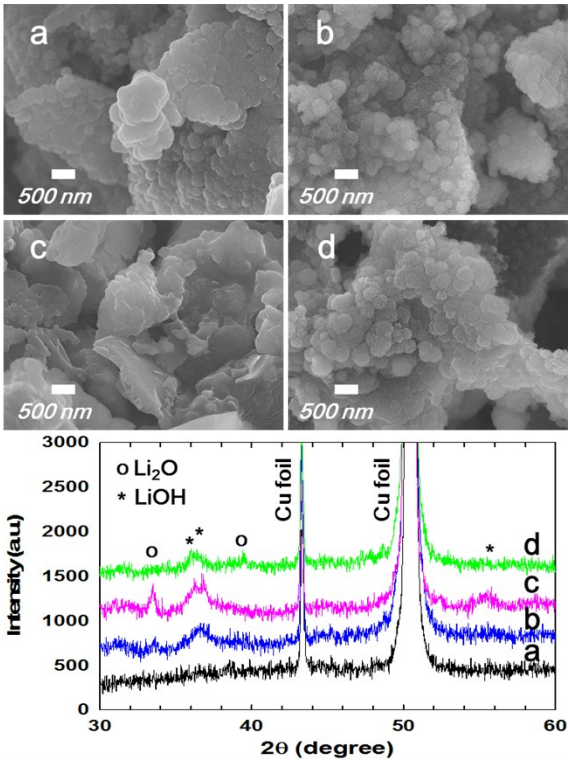

: The crystal morphology and structure of the cycled **MGC** nanocomposites are investigated by FE-SEM and powder XRD analyses. As shown in the top panel of **Fig. S10**, all the cycled derivatives experience significant morphological change during the cycling. In comparison with the clay-incorporated nanocomposites, the clay-free **MGC0** material shows more tightly-aggregated particles, which is partly responsible for its inferior electrode performance over the clay-incorporated materials. Powder XRD patterns of all the present nanocomposites display the diffraction peaks of Li_2O phase generated from the reaction between lithium ions and oxygen in metal oxide, reflecting the formation of Li_2O and amorphous metal and metal oxide phases. This

is common for many metal oxide anode materials working in terms of conversion mechanism. Additionally, the Bragg reflections of LiOH are discernible for the clay-incorporated nanocomposites, indicating the formation of LiOH phase via the decomposition of electrolyte and also the formation of a polymeric gel-like film on the surface of clay nanosheets. This would be related to the redox catalytic activity of clay mineral.

Fig. S11. Charge–discharge capacity plots of (a) **MGC0**, (b) **MGC1**, (c) **MGC2.5**, and (d) **MGC5** as anode materials for sodium-ion batteries (NIBs) at current density of 0.05 A g^{-1}.

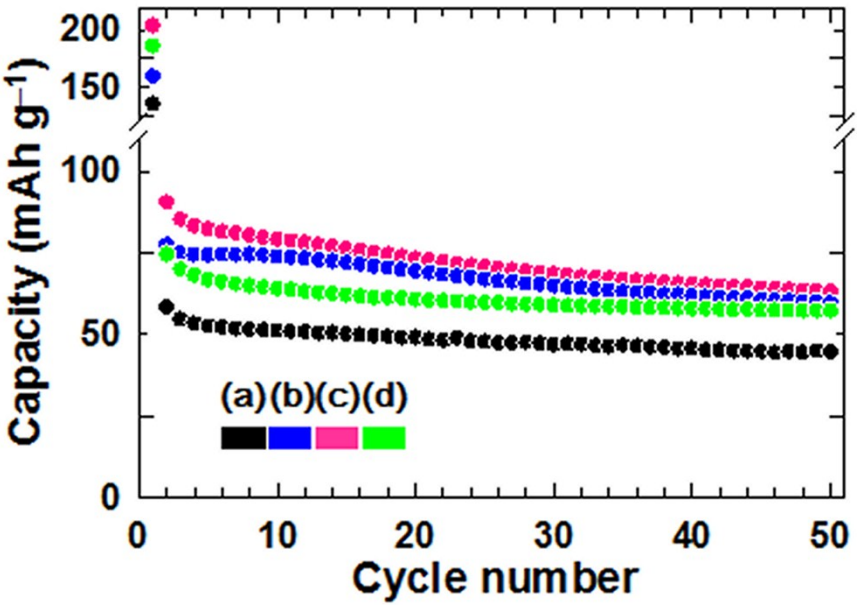

: In addition to the application of lithium ion batteries (LIBs), the present **MGC** nanocomposites are applied as anodes for NIBs to probe the effect of clay addition on the Na ion electrode activity of Mn_3O_4–rG-O nanocomposite. The NIB anode activity of the **MGC** nanocomposite is presented in **Fig. S11**. All the clay-incorporated nanocomposites commonly deliver greater discharge capacities than does the clay-free **MGC0** one, highlighting the beneficial role of clay nanosheet in improving the NIB electrode performance of graphene-based nanocomposites. Among the present materials, the **MGC2.5** nanocomposite shows the best performance as NIB anode.

Table S1. The lattice parameters and crystallite sizes of Mn_3O_4 crystals in the **MGC** nanocomposites estimated by the least squares fitting analysis[a] and Scherrer equation[b], respectively.

Material	Calculated lattice parameter[a]			Estimated crystallite size (nm)[b]
	a (Å)	b (Å)	c (Å)	
MGC0	5.7825	5.7825	9.4494	14
MGC1	5.7771	5.7771	9.4595	13
MGC2.5	5.7858	5.7858	9.4526	14
MGC5	5.7765	5.7765	9.4242	11

: As listed in **Table S1**, the lattice parameters of Mn_3O_4 phase remain nearly the same regardless of clay content, indicating that the incorporation of exfoliated clay nanosheet has negligible effect on the crystal growth of Mn_3O_4. Also, the particle size calculation based on Scherrer equation clearly demonstrates that all the **MGC** nanocomposites have small particle size of 11–14 nm for Mn_3O_4 crystal, reflecting a negligible change of Mn_3O_4 particle size upon the addition of clay nanosheet.

Table S2. The fitted parameters obtained from the electrochemical impedance spectroscopy (EIS) data.

Material	R_s (Ω)	R_f (Ω)	C_f (μF)	R_{ct} (Ω)	C_{dl} (μF)	σ_w (Ω $s^{-1/2}$)	D_{Li+} (cm s^{-1})
MGC0	6.46	98.55	7.63	911	19.04	481.3	3.79×10^{-18}
MGC1	4.10	15.96	35.17	544	13.42	333.6	7.86×10^{-18}
MGC2.5	5.41	15.20	20.38	419	13.21	235.5	1.59×10^{-17}
MGC5	5.94	11.43	20.58	451	15.69	331.4	8.01×10^{-18}

: As can be found from the fitting results for the EIS data in **Table S2**, the **MGC2.5** nanocomposite possesses both the smallest charge-transfer resistance (R_{ct}) and the fastest lithium-ion diffusivity (D_{Li+}), supporting its superior electrode performance over the other electrodes. This result reflects the optimized pore structure of the **MGC2.5** nanocomposite, which is responsible for the enhancement of electrode performance upon the addition of clay nanosheet.